Measuring and modeling twilight's Belt of Venus

Raymond L. Lee, Jr.

Mathematics and Science Division, United States Naval Academy, Annapolis, Maryland 21402, USA (raylee@usna.edu)

Received 11 August 2014; accepted 6 October 2014;
posted 21 October 2014 (Doc. ID 220633); published 13 January 2015

The Belt of Venus (or antitwilight arch) is a reddish band often seen above the antisolar horizon during clear civil twilights, and immediately beneath it is the bluish-gray earth's shadow (or dark segment) cast on the atmosphere. Although both skylight phenomena have prompted decades of scientific research, surprisingly few measurements exist of their spectral, colorimetric, and photometric structure. Hyperspectral imaging of several clear twilights supplies these missing radiometric details and reveals some common spectral features of the antisolar sky at twilight: (1) color differences between the dark segment and the sunlit sky above the antitwilight arch are small or nil; (2) antisolar color and luminance extremes usually occur at different elevation angles; and (3) the two twilight phenomena are most vivid for modest aerosol optical depths. A second-order scattering model that includes extinction by aerosols and ozone provides some preliminary radiative transfer explanations of these twilight features' color and brightness.

OCIS codes: (010.1290) Atmospheric optics; (010.1310) Atmospheric scattering; (010.3920) Meteorology; (290.1090) Aerosol and cloud effects; (330.1730) Colorimetry; (010.1690) Color.
http://dx.doi.org/10.1364/AO.54.00B194

1. Introduction

Vivid, high-purity colors near the solar horizon are a common sight in clear skies during civil twilight. Easily overlooked then are the antisolar horizon's pastel colors, whose more modest gamut includes the reddish Belt of Venus (or *antitwilight arch*) and the bluish-gray earth's shadow (or *dark segment* [1]) beneath it. The etymology of these two twilight features is no less subtle: the planet Venus and the Belt of Venus are only indirectly related, and the earth's shadow on the atmosphere does not fully explain the dark segment.

In particular, atmospheric extinction consistently makes the dark segment's angle with the astronomical horizon larger than the corresponding angles of the solar depression and earth's geometrical shadow. Surface-based observers with a level horizon can even see the dark segment's upper edge just before sunset [2] (say, when refracted sun elevation $h_0 \sim +0.5°$). Nonetheless, this twilight feature's underlying cause is the earth's shadow cast on the atmosphere [3]. Bearing in mind the important distinction between geometrical and extinction-caused shadow boundaries, we can treat "earth's shadow" and "dark segment" as synonyms.

At first glance, the antisolar Belt of Venus seems unrelated to the planet Venus, which only appears in the solar sky within ~47° of the sun [4]. In fact, the term comes from a minor detail of Greco–Roman mythology, in which the literal belt or girdle of Venus was a prized divine adornment that aroused irresistible desire for anyone who wore it [5,6] . How then did this encircling belt come to mean a semicircular arch? Although the modern Belt of Venus' origins are uncertain, one plausible explanation appears in Fig. 1, where the antitwilight arch is clearly part of a *band* of reddened skylight that encircles the horizon and within which Venus could be seen. Because naked-eye observations subtend much smaller angles than fisheye images, everyday visual experience tends to divide the twilight sky into sections. As a result, naked-eye observers could easily reduce the circumhorizontal Belt of Venus to its antisolar half.

Whatever their etymology, the earth's shadow and Belt of Venus have prompted a wide range of

1559-128X/15/04B194-10$15.00/0

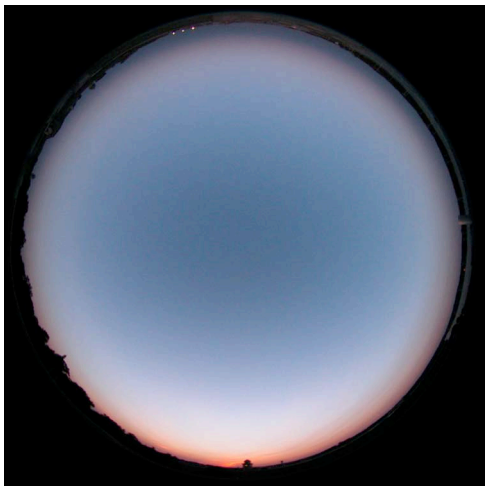

Fig. 1. Fisheye photograph of a clear twilight sky taken at the United States Naval Academy (USNA) in Annapolis, Maryland on 5 September 2002 at 1937 EDT when the unrefracted sun elevation $h_0 = -2.17°$. The dark segment and antitwilight arch are at image top.

qualitative popular explanations [7–12] and quantitative radiative transfer models. In 1951, Dubois claimed that his spectrophotometry of the earth's shadow showed it "is only caused by selective absorption of ozone for [wavelengths] corresponding to the Chappuis band" [13]. Hulburt's 1953 paper demonstrated that ozone's absorption spectrum was also vital to correctly modeling colors and spectra in sunlit regions of the twilight sky, including at the zenith [14]. Rozenberg's 1966 single-scattering equations are an early attempt to model the dark segment and antitwilight arch [15]. While Rozenberg recognizes that multiple scattering is necessary to any truly satisfactory model, he somberly notes that "the introduction of multiple scattering, not to mention reflection from the earth's surface, raises as yet almost insuperable difficulties" [16]. At the time, Divari and Plotnikova partially addressed these difficulties with a second-order scattering model of twilight that also included ozone absorption [17]. Dave and Mateer found in 1968 that single scattering alone could not produce realistic chromaticities in their simulated antitwilight arch and dark segment [18]. In 1974, Adams *et al.* also concluded that their model's twilight chromaticities were limited by its reliance on single scattering, and so they did not attempt to calculate colors for either the dark segment or antitwilight arch [19].

Although computing speeds have increased many orders of magnitude since these landmark studies, speed by itself has not eliminated all of Rozenberg's "almost insuperable" difficulties. Even the fastest computers do not make analytical modeling of higher-order multiple scattering simple, especially in the spherical-shell atmospheres required for twilight models. As a result, researchers have long used Monte Carlo and other techniques to reproduce multiple scattering during twilight [20–28], and many other 3D radiative transfer models can simulate twilight radiance distributions [29–33]. Almost as numerous are papers on twilight spectral radiances measured with photometers and radiometers [34–37], as well as research on naked-eye color matching [38–40] and on colorimeter and photographic measurements of object and sky colors during twilight [41–44]. Despite this wealth of observed and simulated twilight colors, still unanswered are the most basic questions about the antitwilight arch and dark segment: just what are their measured spectra, colors, and luminances, and what radiative-transfer insights can a model provide about these measurements?

2. Measuring the Antisolar Twilight Sky's Spectra, Colors, and Luminances

To answer the first question, I used a Pika II imaging spectrometer [45] to map visible-wavelength radiance spectra during several civil twilights. The Pika II hyperspectral imaging system measures radiances from ~380–910 nm with a spectral resolution of ~4.5 nm and has an analog–digital brightness resolution of 12 bits for each of its 120 spectral channels. In this paper, I only analyze spectral radiances at visible wavelengths λ from 400 to 700 nm. The Pika II's 8 mm Schneider lens has a nominal FOV ~33.4°, and each hyperspectral line of pixels subtends a linear angle ~0.045° wide. System manufacturer Resonon, Inc. provided an absolute radiometric calibration for the Pika II. Each of the 640 pixels that make one vertical scanline has its own spectral calibration, and the calibration procedure follows National Institute of Standards and Technology recommendations. Additional system details are given in [46].

On 12 clear evenings from November 2012 to April 2014, I measured twilight spectra of clear skies at two coastal sites: the United States Naval Academy (USNA) in Annapolis, Maryland, and North Beach, Maryland, both of which are on the western shore of the Chesapeake Bay. For each scan, the camera's optical axis panned along an almucantar at a fixed view-elevation angle $h = 15°$–$16°$ above the astronomical horizon. A calibrated digital inclinometer with a repeatability of $\pm 0.1°$ was used to determine h, and each scan's lateral width of 196° included the solar and antisolar skies. Four of these scans are arranged in Figs. 2(a)–2(d) in order of decreasing aerosol optical depth τ_{aer} for unrefracted $h_0 \sim -3°$ [47]. Because Figs. 2(b) and 2(d) include a wide, unobstructed view of the Chesapeake Bay, I used their astronomical horizons (including a small dip-angle correction [48]) to refine inclinometer measurements of the camera's h angle. In each Fig. 2 scan, $h \sim 30°$ at image top.

Spectral $\tau_{\text{aer},\lambda}$ corresponding to Figs. 2(a)–2(d) are plotted in Fig. 3. These spectra are derived from sun photometer data acquired at nearby Goddard Space Flight Center in Greenbelt, Maryland at the observing times that are closest to those in Fig. 2 [49]. Figure 3's spectra span the entire range of visible wavelength τ_{aer} that occurred during all 12 twilight

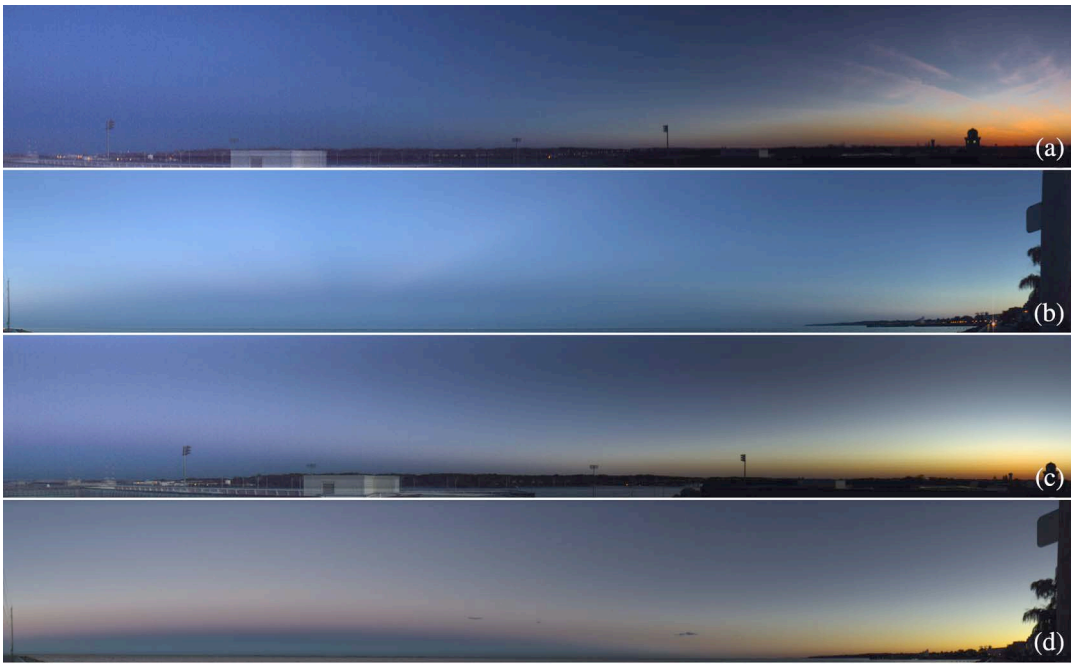

Fig. 2. Visible-wavelength images calculated from hyperspectral scans made along almucantars of view-elevation $h = 15°$–$16°$ for (a) USNA on 3 April 2013 at unrefracted $h_0 = -3.19°$. (b) North Beach, Maryland on 2 October 2013 at $h_0 = -3.14°$. (c) USNA on 1 May 2013 at $h_0 = -2.90°$. (d) North Beach on 3 November 2013 at $h_0 = -2.78°$.

scans, ranging from a maximum on 3 April 2013 [Fig. 2(a)] to a minimum on 3 November 2013 [Fig. 2(d)]. As other authors have noted, the antitwilight arch is most conspicuous when τ_{aer} and its associated slant-path optical thicknesses are not too large [50]. Thus although *some* spectrally selective extinction is needed to create the antitwilight arch's reds, too much extinction (*i.e.*, large τ_{aer}) will reduce its color and luminance contrast to invisibility.

Although Fig. 2(a)'s solar sky is not cloud-free, no thin cirrus are seen beyond the zenith in concurrent fisheye images, nor do Pika II scans exhibit any significant radiometric irregularities above Fig. 2(a)'s antisolar horizon. Yet even when subvisual cirrus *do* subtly influence skylight patterns there, these literally invisible clouds need not be rejected as radiometric contaminants. Because absolutely cloudless skies (including those with no sunlit clouds beyond the solar horizon) are the exception at my coastal sites, nearly clear skies with only a few thin clouds are well worth including in any survey of twilight chromaticity and radiance patterns.

To illustrate this point, examine Fig. 4's time-lapse sequences of antisolar twilights. In Fig. 4(a) (Media 1) from 1 May 2013, the dark segment and antitwilight arch (ATA) steadily increase in h as evening twilight progresses. At the same time, the luminance and color contrasts between them decrease until the ATA disappears at $h_0 \sim -4.7°$. Compare that orderly progress with Fig. 4(b) (Media 2) from 24 September 2013, where anticrepuscular rays begin to intersect the ATA at $h_0 \sim -1.8°$ and thereafter rapidly rotate clockwise across it as the azimuths of the sun and cloud shadows change in unison. In Fig. 4(b) (Media 2), sections of the ATA disappear whenever their region of antisolar sky is shaded from direct sunlight, and they reappear as soon as the cloud shadow moves. Although no clouds are visible anywhere in all-sky images taken on 24 September 2013, these photographs do show crepuscular rays stretching across the entire sky. Given that such shadows are not always seen in local twilights, they

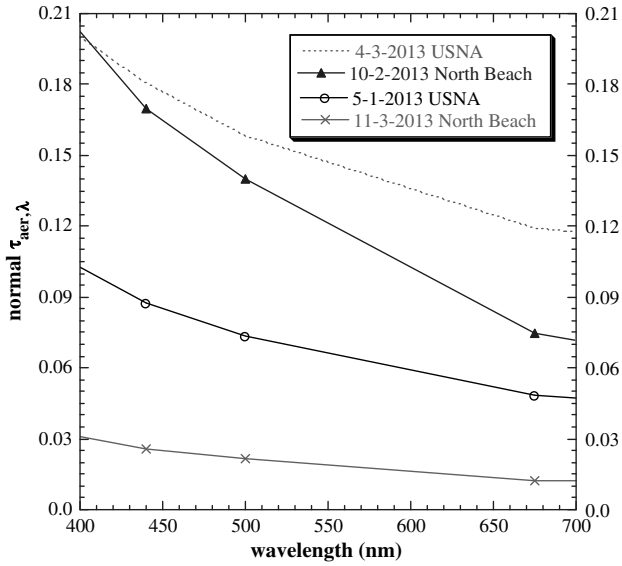

Fig. 3. Aerosol normal optical depths $\tau_{aer,\lambda}$ measured by the NASA Goddard Space Flight Center's AERONET sun photometers at times closest to scans in Fig. 2. Although site names in Fig. 2 are added to line labels, all $\tau_{aer,\lambda}$ spectra were acquired at nearby Greenbelt, Maryland.

Fig. 4. Temporal evolution of the antitwilight arch (ATA) and dark segment in time-lapse sequences made at USNA on (a) 1 May 2013 (Media 1), and (b) 24 September 2013 (Media 2). Within each dark segment starting at $h_0 \sim -4°$, forward scattering of reddened light from the solar sky forms a lower ATA. In Fig. 4(b), changing patterns of anticrepuscular rays make parts of the upper ATA disappear and then reappear.

are likely caused by clouds or spatial variations in haze beyond the solar horizon rather than by topography there [51]. Note too in Figs. 4(a) and 4(b) the dim reddish band that first appears within the dark segment at $h_0 \sim -4°$. Although this antisolar band is not visible in every clear twilight, it is common enough to merit a name, for which I suggest "lower antitwilight arch" [52].

Figure 5's close-up view of the CIE 1976 uniform-chromaticity-scale (UCS) diagram shows colorimetric signatures typical of the antitwilight arch and dark segment as measured along the antisolar meridian (*i.e.*, at relative azimuth $\phi_{\text{rel}} = 180°$). To provide some points of reference, Fig. 5 includes part

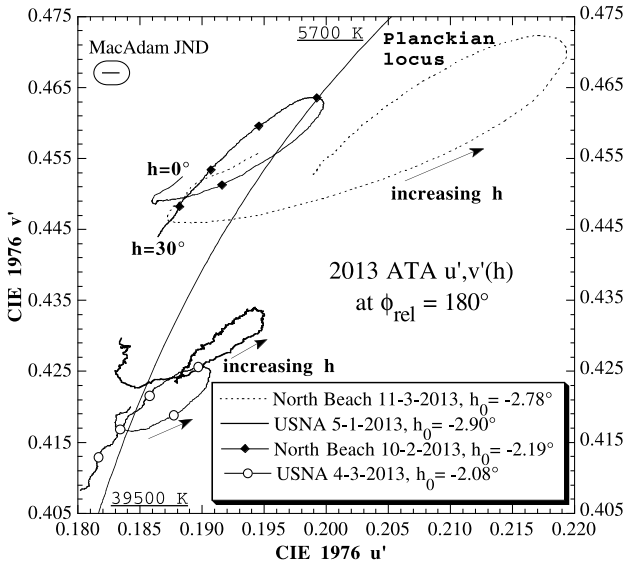

Fig. 5. Smoothed meridional chromaticity curves of the ATA and dark segment for similar h_0 at USNA and North Beach in four different twilights. See Fig. 3 for the corresponding $\tau_{\text{aer},\lambda}$ spectra. Relative azimuth $\phi_{\text{rel}} = 180°$ for all curves, which follow counterclockwise u', $v'(h)$ paths as view-elevation h increases from 0° to 30°.

of the Planckian locus and its corresponding color-temperature limits. Figure 5's perceptual scale for color difference is a MacAdam just-noticeable difference (JND) calculated for this region of the UCS diagram and drawn at the upper left. Qualitatively, Fig. 5's v' ordinate is a light source's proportion of blue to yellow-green (smaller v' is bluer), and its u' abscissa is the proportion of bluish-green to red (larger u' is redder). Alternatively, correlated color temperature (CCT) can be used as a proxy for a source's spectral energy distribution [53,54].

Although very different in their colorimetric gamuts [55] and absolute chromaticities, Fig. 5's four meridional chromaticity curves do share some common traits. Each such curve is a sequence of line segments that connects u', v' chromaticity coordinates at adjacent h. To reduce Pika II pixel noise, each plotted u', v' pair is first smoothed by a uniform, centered filter that operates on the pair and its 14 immediate neighbors. The resulting u', $v'(h)$ chromaticity curves map the h dependence of twilight colors from $h = 0°$ (or the lowest h above local topography) to $h = 30°$ near the top of Fig. 2's scans. Despite large chromaticity differences in τ_{aer} among Fig. 5's four days, each of its u', $v'(h)$ curves traces a similar path: colors are bluest a few degrees above the horizon (*i.e.*, smallest v' and maximum CCT in the dark segment), increase to maximum redness several degrees higher (*i.e.*, minimum CCT in the antitwilight arch), and then grow bluer at still higher h (*i.e.*, in the sky above the ATA).

Such antisolar u', $v'(h)$ curves often form closed loops. This has a surprising implication: colorimetrically speaking, skylight above the ATA closely resembles (and sometimes is identical to) that in the dark segment. Thus, no matter how compelling our visual sense that the dark segment is a very different blue than higher-h skylight, the two sources differ mostly in luminance rather than in hue or CCT. During the day, we seldom see such angularly abrupt changes in

Table 1. Scan Date, CIE 1976 Mean u', v', Normalized Colorimetric Gamut $\hat{g}$, and Unrefracted h_0 for Fig. 5's Four u', $v'(h)$ Chromaticity Curves, with Rows Sorted in Order of Decreasing Normal Optical Depth $\tau_{aer,\lambda}$ at 440 nm

Date (day, month, year)	Mean u'	Mean v'	$\hat{g}$	h_0	$\tau_{aer,\lambda}$(440 nm)
3 April 2013	0.18503	0.41832	0.018950	−2.08°	0.180648
2 October 2013	0.19183	0.45395	0.024196	−3.14°	0.169660
1 May 2013	0.18992	0.42852	0.016076	−2.90°	0.087424
3 November 2013	0.20488	0.46029	0.038792	−2.78°	0.025958

the clear sky's luminance, and this may lead to our color-matching error in the dark segment. In fact, its colorimetric similarity to other blue sky at twilight is no metameric coincidence: the two kinds of skylight are nearly spectrally identical, as shown below.

At similar h_0, the $h = 0° - 30°$ colorimetric gamut in Fig. 5 *tends* to increase with decreasing τ_{aer} (see Table 1). Although the maximum $\tau_{aer,\lambda}$ on 3 April 2013 is paired with small $\hat{g}$, the minimum $\hat{g}$ actually occurs on 1 May 2013 when $\tau_{aer,\lambda}$ has intermediate values. Conversely, a large aerosol optical depth does not always yield the most limited gamut of antisolar skylight colors, as seen in Fig. 5's u', $v'(h)$ curve for 2 October 2013. This same curve also shows that large $\tau_{aer,\lambda}$ does not guarantee an antitwilight arch with the least-reddish (*i.e.*, highest CCT) colors. The vertical distribution of aerosols and ozone may be as important in determining antisolar colors and their gamuts, and modeling addresses this possibility in Section 3. On balance, Fig. 5 adds nuance to, but does not overturn, the existing maxim for surface observers: less turbid daytime skies usually produce the most vivid antisolar twilight colors. For example, Table 1's data suggest that these optimal colors occur for $0.02 \le \tau_{aer}(440\text{ nm}) \le 0.05$.

During the ~35 min that civil twilights last at midlatitudes, aerosol and ozone optical depths and distributions will seldom undergo large-scale changes. As a result, the progression of antisolar colors and colorimetric gamuts during any given clear-sky twilight will hold fewer surprises—once we know what a typical progression is. Based on my measurements, Fig. 6 is a typical sequence of u', $v'(h)$ curves as a function of h_0 in a low-turbidity atmosphere. On Fig. 6's $h_0 = -2.78°$ curve, the ATA and dark-segment color extremes are labeled CCT_{min} and CCT_{max}, respectively. As evening twilight advances, the colors of both these features get bluer, and their combined gamut steadily shrinks from = 0.055410 at $h_0 = -1.56°$ to = 0.016898 at $h_0 = -4.86°$, a decrease of ~70%. Yet even as the antisolar sky's color wanes in Fig. 6, it exhibits a consistent pattern of (1) u', $v'(h)$ curving counterclockwise with increasing h and (2) blues at high h that closely resemble those of the dark segment.

At the two lowest h_0 (−3.87° and −4.86°) in Fig. 6, we can see colorimetric evidence of the lower ATA emerging within the dark segment: near $u' = 0.195$, $v' = 0.448$ are two inverted chromaticity hooks. These stationary points in CCT are signatures of the reddening that is occurring just above the horizon and which helps to define the lower ATA visually. The chromaticity hook is more closed at the lowest $h_0 = -4.86°$, indicating that skylight is more distinctly reddened then. However, this maximum reddening within the dark segment occurs just above Fig. 2(d)'s horizon at $h = 0.4°$, far below the elevation angle of the local maximum in luminance L_v. For comparison, examine the image labeled $h_0 = -4.82°$ in Fig. 4(b) (Media 2) from 24 September 2013. There the lower ATA's maximum L_v occurs ~ halfway up the red and white towers visible near image center, and the corresponding $h \sim 3.3°$.

In fact, local maxima and minima in twilight CCT and L_v seldom coincide in h, nor should we expect them to. In any restricted area of the sky, a maximum-energy spectrum that produces the *brightest* skylight usually differs perceptibly from the maximum-bias spectrum that produces the *most colorful* skylight. For example, Fig. 7 plots a meridional luminance profile $L_v(h)$ through Fig. 2(d)'s dark segment (marked CCT_{max} in Fig. 6) and ATA (marked CCT_{min}). To show more angular detail in Fig. 7's profile measured at lower h_0, its luminances are scaled by a factor of 3.2 (*i.e.*, divide plotted L_v by 3.2 to calculate actual luminances). With this scaling, a local maximum in L_v is clearly visible at $h \sim 2.3°$, and this defines the lower ATA's peak luminance. At such low light levels (~12 cd/m^2 without scaling), observers are more likely to identify this feature from its

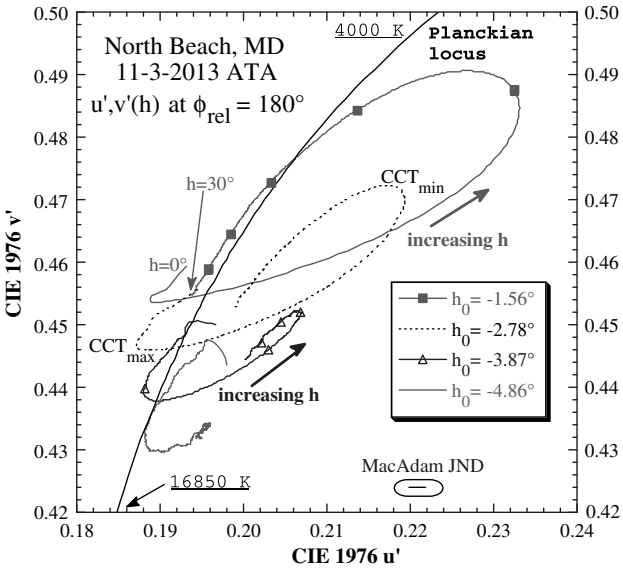

Fig. 6. Smoothed meridional chromaticity curves of the ATA and dark segment as functions of h_0 at North Beach on 3 November 2013. For all curves, $\phi_{rel} = 180°$ and $h = 0°$–$30°$.

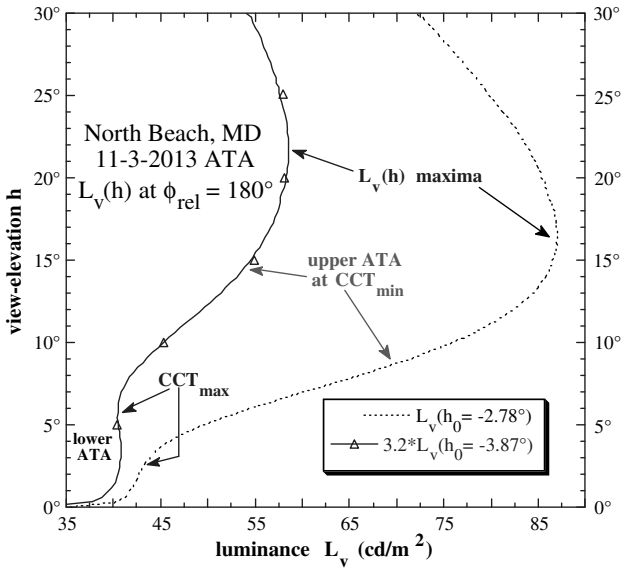

Fig. 7. Smoothed antisolar luminance $L_v(h)$ profiles for the ATA and dark segment at two different h_0 on 3 November 2013 at North Beach. Note that the color extremes CCT_{min} and CCT_{max} (also shown in Fig. 6) do not coincide with local maxima in $L_v(h)$.

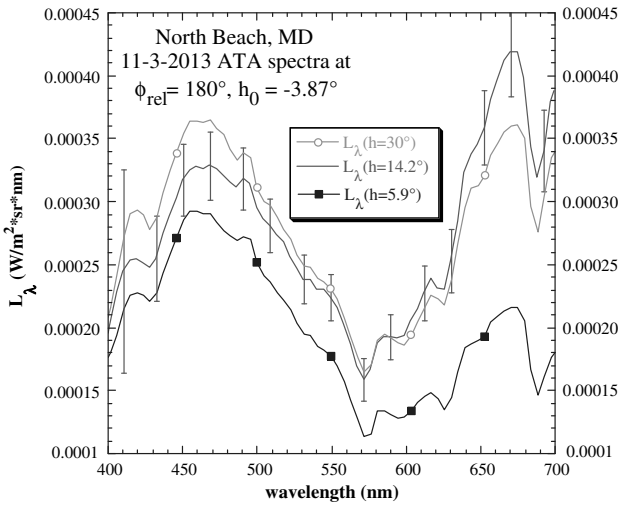

Fig. 8. Radiance spectra for the 3 November 2013 North Beach antisolar twilight; each spectral radiance L_λ is averaged over ~1000 hyperspectral pixels. Shown here are the dark segment's bluest color (at $h = 5.9°$), the ATA's reddest color ($h = 14.2°$), and the bluish sunlit sky above both ($h = 30°$).

maximum L_v rather than from its maximum reddening at $h = 0.4°$.

By comparison, maximum bluing of the dark segment itself (marked CCT_{max} in Fig. 7) occurs well above the lower ATA at $h = 5.9°$. Even more remarkable is the upper ATA's maximum reddening (marked CCT_{min}), which occurs ~6.7° below the $h_0 = -3.87°$ profile's maximum L_v at $h \sim 21°$. Figure 7 also reveals why the lower ATA is not as well defined at $h_0 = -2.78°$; there the $L_v(h)$ profile has no local maximum within the dark segment. As the sun moves farther below the horizon, the luminances and colors of the dark segment and upper ATA rise in Fig. 7.

The Pika II digitized spectral radiances L_λ that underlie these integrated luminances and chromaticities are quite noisy during twilight. Even so, averages of these L_λ help to paint a consistent, remarkably detailed picture of the antisolar twilight sky's spectral structure. Figure 8 shows three such mean radiance spectra from Fig. 2(d)'s distinct dark segment and antitwilight arch. Each L_λ spectrum is an average calculated from $n = 957$ pixels across a digital field-of-view that is 0.62° high by 4.06° wide and centered on the h and ϕ_{rel} of interest. For the $h = 14.2°$ spectrum that corresponds to CCT_{min} of the antitwilight arch, Fig. 8 includes error bars whose half-width is one standard deviation of L_λ over the n pixels.

What new antisolar sky details do these twilight spectra reveal? First, the spectra have strikingly similar shapes and details, including a broad local minimum in L_λ near 600 nm due to absorption by ozone's Chappuis bands. Indeed, all three spectra bear the stamp of this absorption maximum: $L_\lambda(h = 5.9°)$ at CCT_{max} in the dark segment, $L_\lambda(h = 14.2°)$ at CCT_{min} in the upper ATA, and $L_\lambda(h = 30°)$ in the blue, sunlit sky far above. The ATA spectrum differs from the other two because it has just enough additional energy at $\lambda > 630$ nm to redden skylight perceptibly. In comparison, the dark segment and upper skylight L_λ spectra differ chiefly in magnitude rather than in overall shape or spectral details.

So, contrary to Dubois' plausible 1951 claim, the dark segment's spectra (and colors) scarcely differ from those of the sunlit sky above. The spectra in Fig. 8 are not at all unusual, as both the Pika II and another spectrometer (a Photo Research PR-650) consistently record dark-segment spectra that are nearly congruent with those measured at higher h in the same antisolar sky. In hindsight, this close similarity is not surprising: the dark segment is merely other skylight's radiative kin and is produced solely by higher-order scattering from throughout the twilight sky. Indeed, in a multiple-scattering medium with no other light sources than surface reflections (here from the low-reflectivity Chesapeake Bay), we can expect that most antisolar twilight spectra will be minor variations on a single radiative theme.

3. An Approximate Model: Second-order Scattering in the Antisolar Twilight Sky

Knowing that these spectra strongly resemble one another does not help much in predicting their angular distribution. And while existing radiative transfer models can readily calculate these distributions, that output alone does not provide qualitative insights about twilight colors and luminances. A further complication is that the plane-parallel atmosphere assumed by many models (including MODTRAN5 [56]) makes them unusable for twilight studies.

Although MODTRAN's predecessor LOWTRAN7 [57] includes a spherical-shell atmosphere, this

older model has long been obsolete in the sense of not being updated. More importantly in my experience, LOWTRAN sometimes exhibits clearly unrealistic behavior in simulating twilight colors and spectra. More recent and promising candidate models include those of Gedzelman [26], Haber *et al.* [27], and Saito *et al.* [28], but meshing any one of these with my hyperspectral and meteorological data would in itself merit a separate paper. So for the immediate purpose of analyzing twilight chromaticity and luminance (or integrated radiance) trends, I have expanded and updated my own second-order scattering model [58].

The updated multispectral version of this model applies the equation of radiative transfer to a spherical-shell atmosphere in which vertical profiles of aerosol extinction and ozone number density are based on soundings from nearby lidar [59] and Brewer spectrophotometer [60] sites. The model also incorporates surface measurements of normal $\tau_{\mathrm{aer},\lambda}$ such as those in Fig. 3. Scatterers consist of molecules and spherical, absorbing haze droplets, and slant optical pathlengths τ_s are calculated using Bohren and Fraser's algorithm [61]. The model also specifies aerosol size distributions and complex refractive indices, the resulting Mie phase functions, and Lambertian surface reflectances. Although the model does not include ray refraction, calculations show that this omission negligibly affects the angular distribution of scattered twilight radiances, especially for diffuse secondary scattering. Ultimately, the model produces clear-sky L_λ spectra for a surface-based observer as a function of h_0, h, and ϕ_{rel}.

Although calculating secondary scattering is straightforward in principle, in practice it is a fairly slow, complicated exercise, as Rozenberg warily alluded [16]. The most obvious limitation of a second-order model is that it ignores third- and higher-order scattering (*i.e.*, scattering order $N > 2$). However, my independent Monte Carlo calculations indicate that (1) at a visible wavelength of 480 nm, (2) for the range of $\tau_{\mathrm{aer},\lambda}$ encountered in most clear skies, and (3) within the dark segment and antitwilight arch during civil twilight, scattering of order $N > 2$ produces only ~20–25% of the total *diffuse* skylight L_λ. Not including this $N > 2$ scattering in the model does impose some limitations, but experience shows that these can actually be quite instructive.

For example, Figs. 9 and 10 compare measured and modeled chromaticities on two dates with quite different aerosol optical depths: small $\tau_{\mathrm{aer},\lambda}$ on 3 November 2013 and significantly larger $\tau_{\mathrm{aer},\lambda}$ on 2 October 2013 [see Figs. 2(d), 2(b), and 3]. In Fig. 9, the low-turbidity case of 3 November 2013 has a measured $\hat{g}$ that is 2.0 times as large as that for the high-turbidity case of 2 October 2013, even though the sun is nearer the horizon in the latter case, and this tends to increase $\hat{g}$. Note too that the 3 November 2013 case straddles the Planckian locus, and its chromaticity curve is open rather than closed.

Similar patterns exist in Fig. 10's chromaticity curves from the second-order model. First, $\hat{g}$

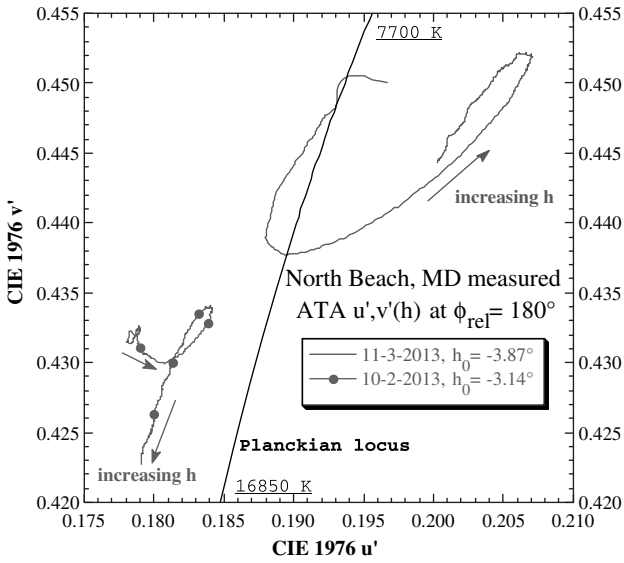

Fig. 9. Smoothed meridional chromaticity curves of the ATA and dark segment measured at similar h_0 during two North Beach twilights, one with large $\tau_{\mathrm{aer},\lambda}$ (2 October 2013) and the other with small $\tau_{\mathrm{aer},\lambda}$ (3 November 2013). For each curve, $\phi_{\mathrm{rel}} = 180°$ and $h = 0°$–$30°$.

calculated using the 3 November 2013 aerosol parameters is 2.14 times as large as that for the 2 October 2013 aerosols, a ratio similar to the observed one. Second, the 3 November 2013 simulated chromaticity curve both straddles the Planckian locus and has an open form. Third, the simulated curve in Fig. 10 for 2 October 2013 is closed, although its shape differs from that measured in Fig. 9. Fourth, small indentations in the modeled u', $v'(h)$ curves in Fig. 10 are the only colorimetric consequence of vertical irregularities in its lidar aerosol profiles,

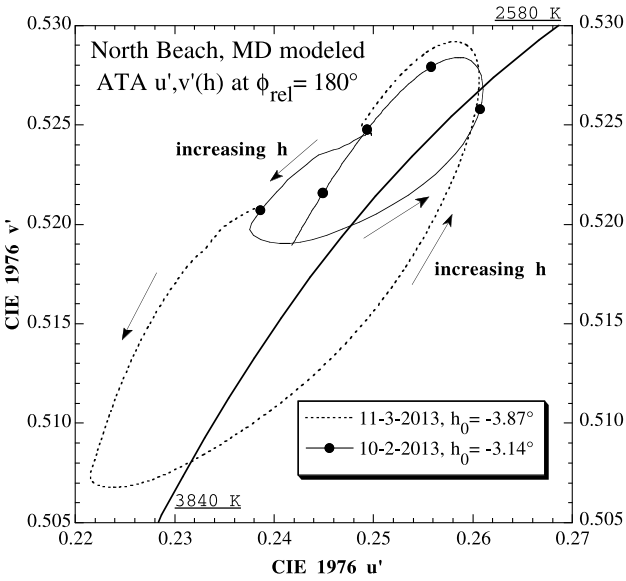

Fig. 10. Meridional chromaticity curves calculated by a second-order scattering model of the ATA and dark segment for atmospheric scattering and absorption conditions similar to those in Fig. 9. For each curve, $\phi_{\mathrm{rel}} = 180°$ and $h = 0°$–$30°$.

and similar indentations appear in the measured chromaticity curves in Fig. 9. Finally, in all measured and modeled cases, antisolar chromaticities follow counterclockwise paths as h increases from 0° to 30°. This last detail is not minor, as it seems to be a persistent (and as yet unexplained) spectral signature of multiple scattering in the dark segment and antitwilight arch.

At the same time, the model differs from nature in some nontrivial ways. First, the second-order chromaticities in Fig. 10 are much redder than their natural archetypes in Fig. 9. Second, in both Fig. 10 cases the model's $\hat{g}$ values are ~2 times as large as their measured counterparts. In fact, calculating absolute chromaticities accurately is difficult for *any* model, and even the thoroughly tested LOWTRAN7 often makes its twilight chromaticity curves unnaturally bluish. Third, unlike the overlapping chromaticity curves simulated in Fig. 10, Fig. 9's measured antisolar chromaticities are distinctly different on the two dates. However, Fig. 5 shows that a few minutes earlier in the 2 October 2013 and 3 November 2013 twilights, their measured chromaticity curves do indeed overlap, so that model predictions at those h_0 better match observations.

The simplest explanation for the first two kinds of errors in the model is its lack of $N > 2$ scattering, which if included would increase skylight radiances at shorter λ. When second-order scattering ($N = 2$) is added to a single-scattering version of the model, its antisolar twilight colors grow much bluer, and so including $N > 2$ scattering can be expected to continue this trend. Including higher-order scattering via Monte Carlo methods should further improve the second-order model's *absolute* chromaticities, even though its existing *relative* chromaticity trends are already fairly realistic. Saito *et al.* have in fact taken such a combined analytic-numerical tack in their JACOSPAR radiative transfer model [28].

Reproducing $L_v(h)$ luminance profiles in the dark segment and antitwilight arch poses fewer problems for the second-order model. In Fig. 2(b), the ATA on 2 October 2013 is visible because of its color contrast over a narrow h interval (see Fig. 5) rather than from the more gradual changes in luminance. Figure 11 plots the 2 October 2013 twilight's measured $L_v(h)$ profile, which has a single maximum at $h \sim 22°$. Figure 12's modeled L_v maximum for 2 October 2013 occurs nearby at $h = 24.4°$. This date's measured and modeled $L_v(h)$ profiles also have quite similar shapes, except for unnaturally rapid changes in simulated $L_v(h)$ near $h = 6°$. The model $L_v(h)$ also have too large a maximum:minimum dynamic range for $h = 0°$–$30°$. The omission of $N > 2$ scattering is the likeliest source of both problems: higher-order scattering would (1) smooth the second-order model's too-rapid transition between the sunlit and shaded sky and (2) increase luminance throughout the dark segment, thereby reducing the $L_v(h)$ profile's overall dynamic range.

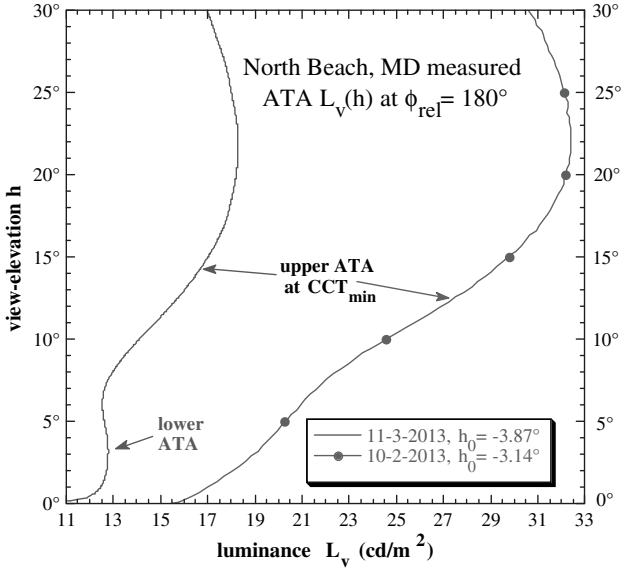

Fig. 11. Smoothed antisolar luminance profiles measured at similar h_0 during two North Beach twilights, one with large $\tau_{aer,\lambda}$ (2 October 2013) and the other with small $\tau_{aer,\lambda}$ (3 November 2013). CCT_{min} indicates the h at which the upper ATA is reddest on each day.

In the 2 October 2013 turbid atmosphere, the lower ATA did not form at any h_0, including at $h_0 = -3.87°$ (see Fig. 6 discussion). By contrast, Fig. 11's local maximum in $L_v(h)$ at $h \sim 3.2°$ on 3 November 2013 marks the elevation of the lower ATA that I saw when $h_0 = -3.87°$. The model's L_v local maximum at $h = 1.6°$ in Fig. 12 is close to this measured h value. The lower ATA is scarcely affected by restricting the model's illumination of the antisolar horizon to just the solar sky ($-90° \le \phi_{rel} \le +90°$). This indicates that the lower ATA is caused by forward

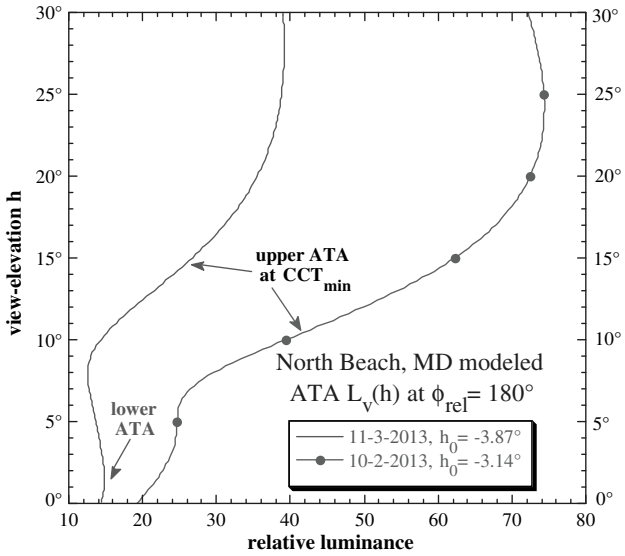

Fig. 12. Antisolar luminance profiles calculated by a second-order scattering model for atmospheric scattering and absorption conditions similar to those in Fig. 11. CCT_{min} indicates the h at which the upper ATA is reddest on each day.

scattering of reddened skylight that illuminates large τ_s near the antisolar horizon. In other words, it is a twilight variation on the horizon brightening seen in clear daytime skies [10,58]. An upper ATA also was visible on 2 October 2013 due to Fig. 2(b)'s reddening at $h = 12.4°$, which is marked on Fig. 11 as CCT_{min}. Comparing h values for minimum CCTs in Figs. 11 and 12 reveals (1) differences of 2° or less in the predicted and observed positions of the upper ATA and (2) more evidence that luminance and color extremes in the ATA are fundamentally independent of one another.

4. Conclusions

Despite decades of scientific study of the antisolar twilight sky, we still know very few details of its combined spectral, colorimetric, and photometric properties. This paper is one step toward identifying those details. First, the dark segment's colors and spectra do not differ fundamentally from the sunlit sky above the antitwilight arch. In fact, much of the antisolar twilight sky bears ozone absorption's spectral imprint, not just the dark segment: its apparently distinctive blue is a perceptual artifact likely caused by its much lower luminance. Second, the upper ATA is distinct because of its color contrast with the dark segment below it, not because of the wide local maximum in luminance above it. Insofar as we can identify the upper arch's ill-defined h, it occurs where skylight has a local minimum in CCT.

Third, the antitwilight arch is something of a Goldilocks phenomenon: it requires just the right amount of aerosol to shine. With too little aerosol, direct sunlight on the antisolar sky produces reds (or even yellows) that are quite pastel; with too much aerosol, direct sunlight is reduced so much that the arch's colors are subthreshold. Fourth, a dim, little-noticed reddish band can be seen within the dark segment late in evening civil twilight. This lower antitwilight arch is a fairly common feature in my measurements, but it too can be rendered invisible by aerosol extremes. Because of the lower ATA's near-mesopic luminance levels, often it is detected by luminance contrast rather than color contrast. For example, late in evening civil twilight it remains visible only as a ghostly white glow along the antisolar horizon, even though its spectrum is still reddish.

Determining exactly what aerosol and ozone environments enhance or obscure these naked-eye twilight phenomena is the difficult task that remains for radiative transfer models. Although the second-order scattering model described above is not definitive, unlike some existing models it does account for many visible features of the antisolar twilight sky. Adding higher-order scattering to it or another spherical-shell model will help bring radiative-transfer closure to the Belt of Venus.

Raymond Lee was generously supported by United States National Science Foundation grant AGS-0914535 and by the United States Naval Academy's Departments of Mathematics and Physics. Opinions, findings, and conclusions or recommendations expressed in this paper are those of the author and do not necessarily reflect the views of the National Science Foundation. Thanks go to Jay Herman, Maria Tzortziou, and Gordon Labow of NASA's Goddard Space Flight Center for their efforts in establishing and maintaining its AERONET site and the $\tau_{aer,\lambda}$ data reproduced in Fig. 3.

References and Notes

1. T. S. Glickman, ed., *Glossary of Meteorology*, 2nd ed. (American Meteorological Society, 2000), pp. 47–48, 200, 248.
2. D. K. Lynch and W. Livingston, *Color and Light in Nature* (Cambridge, 1995), pp. 37–38.
3. G. V. Rozenberg, *Twilight: A Study in Atmospheric Optics* (Plenum, 1966), pp. 245–249.
4. M. E. Bakich, *Cambridge Planetary Handbook* (Cambridge, 2000), p. 108.
5. E. E. Barthell, Jr., *Gods and Goddesses of Ancient Greece* (University of Miami, 1971), p. 32. Barthell discusses the cestus (or girdle) of Aphrodite, who was the Greek precursor of the Roman Venus.
6. C. Winterer, "Venus on the sofa: Women, Neoclassicism, and the early American republic," Modern Intellectual History **2**, 29–60 (2005); see note 12, p. 36.
7. W. J. Humphreys, *Physics of the Air* (McGraw-Hill, 1940), pp. 566–567.
8. R. Greenler, *Rainbows, Halos, and Glories* (Cambridge, 1980), pp. 131–132.
9. F. Schaaf, *Wonders of the Sky: Observing Rainbows, Comets, Eclipses, the Stars, and Other Phenomena* (Dover, 1983), pp. 62–63.
10. M. G. J. Minnaert, *Light and Color in the Outdoors* (Springer-Verlag 1993), pp. 296–299.
11. J. C. Naylor, *Out of the Blue: A 24-Hour Skywatcher's Guide* (Cambridge, 2002), pp. 69–72.
12. G. Hoeppe, *Why the Sky is Blue: Discovering the Color of Life* (Princeton, 2007), pp. 253–255.
13. J. Dubois, "Contribution a l'étude de l'ombre de la terre," Ann. Géophys. **7**, 103–107, 145–163 (1951).
14. E. O. Hulburt, "Explanation of the brightness and color of the sky, particularly the twilight sky," J. Opt. Soc. Am. **43**, 113–118 (1953).
15. Refs. [2,3] and [7–13] collectively employ 10 different terms to describe these two twilight phenomena, so for simplicity hereinafter I use only the newer "antitwilight arch" and "dark segment".
16. G. V. Rozenberg, *Twilight: A Study in Atmospheric Optics* (Plenum, 1966), p. 250.
17. N. B. Divari and L. I. Plotnikova, "Computed brightness of the twilight sky," Sov. Astron. **9**, 840–852 (1966).
18. J. V. Dave and C. L. Mateer, "The effect of stratospheric dust on the color of the twilight sky," J. Geophys. Res. **73**, 6897–6913 (1968).
19. C. N. Adams, G. N. Plass, and G. W. Kattawar, "The influence of ozone and aerosols on the brightness and color of the twilight sky," J. Atmos. Sci. **31**, 1662–1674 (1974).
20. D. G. Collins, W. G. Blättner, M. B. Wells, and H. G. Horak, "Backward Monte Carlo calculations of the polarization characteristics of the radiation emerging from spherical-shell atmospheres," Appl. Opt. **11**, 2684–2696 (1972).
21. W. G. Blättner, H. G. Horak, D. G. Collins, and M. B. Wells, "Monte Carlo studies of the sky radiation at twilight," Appl. Opt. **13**, 534–547 (1974).
22. C. N. Adams and G. W. Kattawar, "Radiative transfer in spherical shell atmospheres: I. Rayleigh scattering," Icarus **35**, 139–151 (1978).
23. W. Beiying and L. Daren, "Simulation of the intensity and polarization of skylight during twilight period," Adv. Atmos. Sci. **5**, 15–26 (1988).
24. B. M. Herman, A. Ben-David, and K. J. Thome, "Numerical technique for solving the radiative transfer equation for a spherical shell atmosphere," Appl. Opt. **33**, 1760–1770

(1994). Although Herman *et al.* had not yet adapted their Gauss–Seidel iteration technique to twilight atmospheres, they planned to do so in future research.
25. Yu. E. Belikov, "Modelling of the twilight sky brightness using a numerical solution of the radiation transfer equation," J. Atmos. Terr. Phys. **58**, 1843–1848 (1996).
26. S. D. Gedzelman, "Simulating colors of clear and partly cloudy skies," Appl. Opt. **44**, 5723–5736 (2005).
27. J. Haber, M. Magnor, and H.-P. Seidel, "Physically-based simulation of twilight phenomena," ACM Trans. **24**, 1353–1373 (2005).
28. M. Saito, H. Iwabuchi, and T. Hayasaka, "Physical explanation of tropospheric aerosol effects on twilight sky color based on photographic observations and radiative transfer simulations," Scientif. Online Lett. Atmos. (SOLA) **9**, 15–18 (2013).
29. B. Mayer and A. Kylling, "Technical note: The libRadtran software package for radiative transfer calculations—description and examples of use," Atmos. Chem. Phys. **5**, 1855–1877 (2005).
30. F. Spada, M. C. Krol, and P. Stammes, "McSCIA: Application of the equivalence theorem in a Monte Carlo radiative transfer model for spherical shell atmospheres," Atmos. Chem. Phys. **6**, 4823–4842 (2006).
31. J. Lenoble, M. Herman, J. L. Deuzé, B. Lafrance, R. Santer, and D. Tanré, "A successive order of scattering code for solving the vector equation of transfer in the earth's atmosphere with aerosols," J. Quant. Spectros. Radiat. Trans. **107**, 479–507 (2007).
32. R. Pincus and K. F. Evans, "Computational cost and accuracy in calculating three-dimensional radiative transfer: Results for new implementations of Monte Carlo and SHDOM," J. Atmos. Sci. **66**, 3131–3146 (2009).
33. M. Premuda, E. Palazzi, F. Ravegnani, D. Bortoli, S. Masieri, and G. Giovanelli, "MOCRA: A Monte Carlo code for the simulation of radiative transfer in the atmosphere," Opt. Express **20**, 7973–7993 (2012).
34. O. S. Ougolnikov, "Twilight sky photometry and polarimetry: The problem of multiple scattering at the twilight time," Cosmic Res. **37**, 159–166 (1999).
35. F. E. Volz, "Twilights and stratospheric dust before and after the Agung eruption," Appl. Opt. **8**, 2505–2517 (1969).
36. K. L. Coulson, *Polarization and Intensity of Light in the Atmosphere* (A. Deepak Publishing, 1988), pp. 397–413.
37. R. L. Lee, Jr. and J. Hernández-Andrés, "Measuring and modeling twilight's purple light," Appl. Opt. **42**, 445–457 (2003).
38. W. E. K. Middleton and E. G. Mayo, "The appearance of colors during twilight," J. Opt. Soc. Am. **42**, 116–121 (1952).
39. F. F. Hall, Jr., "Twilight sky colors: Observations and the status of modeling," J. Opt. Soc. Am. **69**, 1179–1180, 1197 (1979).
40. M. G. J. Minnaert, *Light and Color in the Outdoors* (Springer-Verlag 1993), pp. 294–297.
41. M. Gadsden, "The colour of the zenith twilight sky: Absorption due to ozone," J. Atmos. Terres. Phys. **10**, 176–180 (1957).
42. R. L. Lee, Jr., "Twilight and daytime colors of the clear sky," Appl. Opt. **33**, 4629–4638, 4959 (1994).
43. J. Hernández-Andrés, R. L. Lee, Jr., and J. Romero, "Color and luminance asymmetries in the clear sky," Appl. Opt. **42**, 458–464 (2003).
44. R. L. Lee, Jr., W. Meyer, and G. Hoeppe, "Atmospheric ozone and colors of the Antarctic twilight sky," Appl. Opt. **50**, F162–F171 (2011).
45. Pika II hyperspectral imaging system from Resonon, Inc., 619 North Church Avenue, Bozeman, Mont. 59715 (http://www.resonon.com). The system consists of a digital camera that has an internal diffraction grating and is coupled to a rotation stage controlled by a precision stepper motor and laptop computer. In this pushbroom system, the laptop acquires 640 different skylight spectra at each rotation stage position (*i.e.*, for each line of the resulting hyperspectral datacube).
46. R. L. Lee, Jr. and O. R. Samudio, "Spectral polarization of clear and hazy coastal skies," Appl. Opt. **51**, 7499–7508 (2012).
47. During the 3.5 min needed to acquire a scan at twilight lighting levels, h_0 changes by ∼0.65° at Fig. 2's two sites. As a result, each of Fig. 2's vertical scanlines has a slightly different h_0, and this shift is included in all calculations. For display purposes, Figs. 2(a) and 2(c) have been flipped horizontally so the solar sky is on the right, just as it is in Figs. 2(b) and 2(d).
48. A. T. Young and G. W. Kattawar, "Sunset science. II. A useful diagram," Appl. Opt. **37**, 3785–3792 (1998).
49. Fig. 3's $\tau_{\mathrm{aer},\lambda}$ data is archived by the AErosol RObotic NETwork (AERONET) at http://aeronet.gsfc.nasa.gov.
50. See [2], p. 37 and [10], p. 293.
51. For other examples of cloud shadows' effects on twilight colors, see Ref. [37].
52. Minnaert calls this band the "lowest countertwilight" (Ref. 10, p. 297).
53. CCT and the MacAdam JND are described in G. Wyszecki and W. S. Stiles, *Color Science: Concepts and Methods, Quantitative Data and Formulae*, 2nd ed. (Wiley, 1982), pp. 224–225, 306–310.
54. J. Hernández-Andrés, R. L. Lee, Jr., and J. Romero, "Calculating correlated color temperatures across the entire gamut of daylight and skylight chromaticities," Appl. Opt. **38**, 5703–5709 (1999).
55. See Ref. [42] for a quantitative definition of the normalized colorimetric gamut $\hat{g}$.
56. Spectral Sciences, Inc., "Modtran5," http://modtran5.com.
57. The LOWTRAN7 radiative transfer model is described in R. W. Fenn, S. A. Clough, W. O. Gallery, R. E. Good, F. X. Kneizys, J. D. Mill, L. S. Rothman, E. P. Shettle, and F. E. Volz, "Optical and infrared properties of the atmosphere," in *Handbook of Geophysics and the Space Environment*, A. S. Jursa, ed. (Air Force Geophysics Laboratory, Hanscom Air Force Base, 1985), Chap. 18, pp. 44–51.
58. R. L. Lee, Jr., "Horizon brightness revisited: Measurements and a model of clear-sky radiances," Appl. Opt. **33**, 4620–4628, 4959 (1994).
59. Vertical profiles of 527-nm aerosol extinction coefficients are archived by the Micro-Pulse Lidar Network (MPLNET) at http://mplnet.gsfc.nasa.gov/data.html.
60. Vertical profiles of ozone number densities are archived by the NOAA-EPA Brewer Spectrophotometer UV and Ozone Network (NEUBrew) at http://esrl.noaa.gov/gmd/grad/neubrew.
61. C. F. Bohren and A. B. Fraser, "At what altitude does the horizon cease to be visible?" Am. J. Phys. **54**, 222–227 (1986). For $h > 5°$ in their model, τ_s effectively varies as the secant of zenith angle [*i.e.*, $\tau_s \propto 1/\cos(90°-h)$].